Int J Adv Manuf Technol (2015) 79:469–489
DOI 10.1007/s00170-015-6821-z

ORIGINAL ARTICLE

Thermal characteristics analysis and experimental study on the high-speed spindle system

Chi Ma · Xuesong Mei · Jun Yang · Liang Zhao · Hu Shi

Received: 21 September 2014 / Accepted: 18 January 2015 / Published online: 8 February 2015
© Springer-Verlag London 2015

Abstract In order to avoid the sudden failure of high-speed spindles in the actual machining process caused by an excessive temperature rise at the design stage, a three-dimensional (3D) finite element analysis (FEA) model was proposed to conduct transient thermal-structure interactive analysis of a high-speed spindle. The FEA model considered thermal contact resistance (TCR) at solid joints and bearing stiffness to improve the accuracy of traditional thermal models which ignored TCR. However, TCRs at solid joints and bearing stiffness were often ignored in traditional thermal models of high-speed spindles. This caused inaccuracies in traditional thermal models. The heat generation of the built-in motor was calculated based on the efficiency analysis method proposed by Bossmanns and Tu [1]. Based on the quasi-static mechanics analysis of rolling bearing, the heat generation and stiffness of bearings were calculated by applying the Newton-Raphson algorithm to improve the convergence. The Weierstrass-Mandelbrot (W-M) function, a function of fractal parameters, was used to characterize the rough surface morphology of bearing rings. The fractal parameters were identified by the structure function method and the measurement data of bearing ring's surface morphology, and a contact mechanics model was developed to calculate the contact parameters used in the model of TCR. Then, a new predictive model for TCR was proposed based on M-T model. The above boundary conditions were applied to the FEA model, and thermal equilibrium experiments were conducted to validate the effectiveness of the model. The results showed that the FEA model was much more accurate than the traditional model which ignored TCRs at solid joints and bearing stiffness.

Keywords Finite element analysis · Temperature field · Thermal error · Thermal contact resistance · Fractal geometry · Contact mechanics

C. Ma · X. Mei · J. Yang · L. Zhao · H. Shi (✉)
State Key Laboratory for Manufacturing Systems Engineering, Xi'an Jiaotong University, 710049 Xi'an, China
e-mail: tigershi@mail.xjtu.edu.cn

C. Ma
e-mail: ljlmachi@gmail.com

X. Mei
e-mail: xsmei@mail.xjtu.edu.cn

J. Yang
e-mail: softyj@163.com

L. Zhao
e-mail: zl9527@gmail.com

1 Introduction

High-speed and high-precision machining is the development direction of the modern manufacturing industry, and the application of high-speed spindle, a core component of machine tools, is critical for the implementation of high-speed and high-precision machining. Therefore, the efficiency and precision of high-speed spindles have great influence on machining efficiency and accuracy. However, in order to improve the transmission performance, the built-in motor and high-speed bearing are combined in motorized spindles so that a large amount of heat is introduced into spindle systems, and the heat dissipation condition is poor because of its compact structure. Besides, the structure of high-speed spindles is complex, and the material properties of components are different. Therefore, the interactive influence of such factors as heat source's location and intensity, heat dissipation condition, machine tool structure, and material properties may produce complex thermal characteristics. For example, the uneven

distribution of temperature field leads to spindle's thermal errors, and the distribution is nonlinear, nonstationary and varies with time [2], and eventually results in a poor machine tool's machining accuracy. Numerous studies showed that the thermal errors account for 70 % of the total error resulting from various error sources [1–3], and the more sophisticated the machine tool, the greater is the proportion of thermal errors [3]. Therefore, it is essential to investigate the thermal characteristics of high-speed spindles.

In recent years, numerical simulation methods have become a topic of increasing interest and are applied to analyze thermal characteristics of machine tools. The most typical approach is the theory of finite difference method (FDM), finite volume method (FVM), and finite element method (FEM); Bossmanns et al. applied FDM to analyze the heat generation, heat dissipation, and the energy distribution of a high-speed spindle [1]. Su et al. proposed an integrated heat-fluid-solid coupling model of the hydrostatic spindle system based on the finite volume element method (FVEM) in consideration of the interaction of the temperature field, thermal deformation, and eccentricity [4]. Liang et al. studied the thermal behaviors of a machine tool by the FVEM to consider the influence of temperature rise, preload forces, contact surfaces, and gravity and proposed a new thermal optimization method to reduce the thermal error at the design stage [5]. Zivkovic et al. proposed the thermo-mechanical model of a spindle which considered the nonstationary change of temperature and thermal deformation [6]. Kim et al. proposed a simulation method for predicting thermo-elastic behavior of the spindle-bearing system and an optimization procedure for housing design parameters under various spindle-bearing operating and surrounding conditions such as assembling tolerancing, geometric dimensioning, cooling condition, and thermal deformation [7]. Babu et al. used the FEM to gain insights into the extent of the contribution made by the elements of the headstock assembly to the transient temperature rise and the resulting thermal deformation characteristics [8]. Zhang presented whole-machine temperature field and thermal deformation modeling and a simulation method for vertical machining centers to study its thermal characteristics at the design stage [9]. In the models mentioned above, the heat generation and heat transfer, as the important boundary conditions for thermal analysis, are taken into account. However, the influence of TCRs on the simulation results was ignored in these models because the difference between the heat transfers of continuum and joint surface is not identified. And it is unreasonable for some researchers to set the value of TCR as an empirical constant for various joint surfaces because the strongly nonlinear relationship between TCR and such factors as rough surface morphology, interface pressure, contact area, contact deformation modes, material physical properties, and temperature. On the other hand, bearing's axial and radial stiffness have great effect on the thermal deformation of the spindle system. And hence, the bearing's stiffness should be considered when the FEA model is developed. Liu et al. studied the thermal characteristics of a motorized spindle by which considered the effect of TCRs [10]. Su et al. studied the thermal characteristics of an ultra-precision machine tool and proposed a finite element fractal method to consider the influence of TCR on the thermal characteristics by combining the advantages of FEM and fractal theory [11]. However, the combined effect of the morphology of rough surface and contact deformation of asperities on TCR was not considered in the model. In fact, the core of a TCR analysis is its geometry and mechanical issues, and hence, the morphology of rough surface and contact deformation of asperities should not be ignored.

The framework of this paper is arranged as follows. Section 2 introduced the high-speed spindle system. Section 3 proposed the thermal characteristics analysis model and discussed the calculation methods of boundary conditions. In this section, the heat generation of the built-in motor was calculated based on the efficiency analysis method. Then, based on the rolling bearing quasi-static mechanics analysis, Newton-Raphson algorithm was used to calculate the heat generation and stiffness of bearings. The fluid flow state was determined by Reynolds number, and the convective heat transfer coefficients of the spindle's different components were calculated based on the Nusselt number determined by different convective heat transfer models. The W-M function, a function of fractal parameters, was utilized to characterize the rough surface morphology of bearing rings. And the fractal parameters were identified by the measurement data of surface morphology and the structure function method. Elastic, plastic, and elastic-plastic contact deformation modes of two contacting surfaces were considered to develop a contact mechanics model. Then, a TCR model was proposed based on the geometric and mechanical analysis of joint surfaces. Eventually, the spindle thermal model was proposed by applying the above boundary conditions to the FEM model. Section 4 conducted thermal equilibrium experiments to validate the effectiveness of the model. The results of this model were compared with experimental data and traditional thermal model which ignored TCRs and bearing stiffness. The results showed good agreement, demonstrating the validity of the FEA model, and providing certain references for the further study on the machine tool's thermal characteristics. Section 5 presented the conclusions obtained from the previous analysis.

2 Spindle system

The setup to be modeled is a high-speed spindle system designed by our research group, as shown in Fig. 1. The maximum rotational speed of the spindle is 20,000 rpm, and its cooling system can control the temperature variation. Two

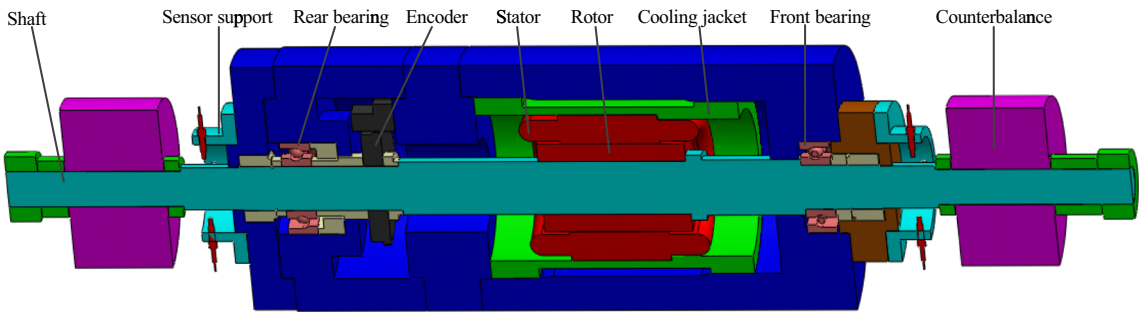

Fig. 1 High-speed spindle model

counterweights are installed on both ends of the spindle to adjust its rotation error. An encoder is mounted on the shaft to feedback the rotational speed. A pair of bearings SKF7005 ACD/P4A are mounted on the spindle with a clearance tolerance to avoid the preload variation due to temperature variation and arranged in a back-to-back layout and preloaded (600 N) by two sleeves and a locknut. Four temperature sensors are installed to measure the temperatures of the front and rear bearings, cooling jacket, stator, spindle housing, and ambient. The material properties of the spindle components are listed in Table 1.

3 Finite element analysis

To get accurate numerical solutions of temperature field and thermal deformation of the spindle system, the solid structure should be reasonably simplified and finely meshed. Moreover, the credibility of the simulation results also relies on whether the boundary conditions such as the heat sources, convective heat transfer coefficients, TCRs of solid joints, and bearing stiffness are well defined.

The control equation of transient thermal analysis can be expressed as

$$\rho c\frac{\partial T}{\partial t}=\frac{\partial}{\partial x}\left(\lambda_x\frac{\partial T}{\partial x}\right)+\frac{\partial}{\partial y}\left(\lambda_y\frac{\partial T}{\partial y}\right)+\frac{\partial}{\partial z}\left(\lambda_z\frac{\partial T}{\partial z}\right)+Q \quad (1)$$

where $T=T(x,y,z,t)$ denotes the temperature of each element (°C); ρ and c are the material's density (kg/m^3) and specific heat capacity (J/(kg °C)), respectively; t denotes time (s), λ_x, λ_y, and λ_z denote material's thermal conductivity in the x, y, and z directions, respectively (W/(M·K)); and Q denotes the internal heat source (W/m^3).

Thermal deformation is calculated based on Hooke's law

$$\varepsilon=\alpha\cdot\Delta T \quad (2)$$

where ε is the strain vector, α is the material's thermal expansion coefficient, and ΔT denotes the temperature rise vector.

3.1 Finite element modeling

The solid model of spindle system is built, and some small structures are simplified due to their little influence on the simulation results, such as thread hole, key groove, chamfer, and fillet. Considering the high rotational speed of the spindle, the bearing can be simplified as a hollow cylinder. The simplified model is imported to ANSYS Workbench, and the hexahedral element with 20 nodes is adopted to mesh the solid structure. In order to get good simulation results, the region with larger temperature gradient is meshed more refined, such as the region near the motor and bearings. There are a total of 298,147 solid elements and 1165,218 nodes in the FEA model, as shown in Fig. 2.

The TCRs of those joints except those formed by bearing/bearing housing and bearing/shaft are ignored because of their little influence on the thermal characteristics of the spindle system. Namely, there are four joints in the spindle system, as shown in Fig. 3. To simulate the joints, contact pairs are created at the solid joints and TCR is applied to each joint surface, which is to be explained below. And the predictive

Table 1 Material properties of the spindle components

Materials	Density (kg/m^3)	Coefficient of thermal expansion (μm/(°C))	Young's modulus (GPa)	Poisson's ratio	Thermal conductivity (W/(m·K))	Specific heat capacity (J/(kg·°C))
GCr15SiMn	7810	12.5	207	0.3	60.5	460
38CMoAl	7860	9.7	200	0.31	65.5	485
3Cr13	7750	10.2	200	0.29	28.5	502

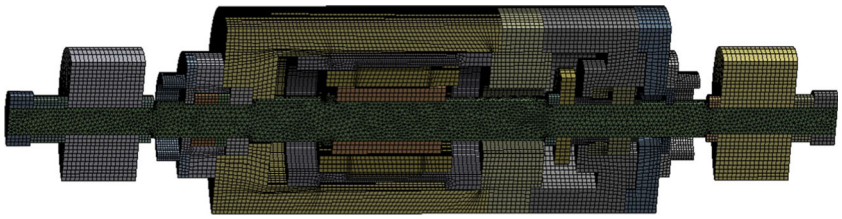

Fig. 2 Finite element model

model for TCR is proposed based on M-B fractal contact model to overcome the shortages of other models.

3.2 Heat loads of the high-speed spindle system

3.2.1 Heat generation of the built-in motor

It is difficult to calculate the copper loss, iron loss, and other additional loss of the built-in motor accurately. Therefore, the motor's efficiency analysis method is used to calculate the heat generation of the built-in motor. The air resistance loss P_{windge} can be expressed as

$$P_{\text{windage}} = \pi^3 \cdot d_{\text{rotor}}^3 \cdot L_{\text{rotor}} \cdot \mu_{\text{air}} \cdot f_{\text{rotor}}^2 \Big/ h_{\text{gap}} \tag{3}$$

where d_{rotor} and L_{rotor} denote the rotor's outer diameter and length, respectively; h_{gap} is the thickness of the gap between rotor and stator; μ_{air} denotes air's dynamic viscosity; and f_{rotor} denotes rotor's rotational frequency.

The efficiency of the built-in motor is defined as [12]

$$\eta = \left(P_{\text{out}} + P_{\text{bearing}} + P_{\text{windage}}\right) \Big/ P_{\text{in}} \tag{4}$$

where P_{bearing} denotes bearing's heat power and the calculation method will be discussed in detail in Section 3.2.2, P_{out} is the output of the mechanical energy, when the spindle is air cutting, P_{out} is zero, P_{in} denotes the input power of the motor, and η is the efficiency of the motor.

The motor's heat generation Q can be obtained according to Eqs. (3) and (4).

$$Q = P_{\text{in}}(1-\eta) + P_{\text{windge}} \tag{5}$$

The distribution of the motor's heat generation between the rotor and stator is determined by the synchronous frequency f_{sync} and slip ratio f_{slip} [12], as shown in Eq. (6).

$$\begin{cases} Q_{\text{rotor}} = Q \cdot \dfrac{f_{\text{slip}}}{f_{\text{sync}}} \\ Q_{\text{stator}} = Q - Q_{\text{rotor}} \end{cases} \tag{6}$$

where Q_{rotor} and Q_{stator} denote the heat generation of the rotor and stator, respectively.

3.2.2 Heat generation of bearing

The traditional method to calculate the heat generation of bearing is quasi-static mechanics analysis. The geometric, physical, balls, and rings balance equations constitute of balance equation set of bearing. Figure 4 depicts the force applied to the rolling elements. Under the combined effect of all external loads, the relative position between the curvature centers of the inner ring and rolling elements is shown in Fig. 5. Centrifugal force and gyroscopic moment are also applied to the rolling elements at high speeds, and the contact angles of rolling elements and inner with outer rings will also change. Therefore, the positions of the curvature centers of the inner ring and balls change from point m to m' and point E to E', respectively.

The geometric equations can be obtained according to the geometric relationship shown in Fig. 5

$$\begin{aligned} A_{xq} &= BD_w \sin\alpha_0 + \delta_a + \theta R_i \cos\psi_q \\ A_{zq} &= BD_w \cos\alpha_0 + \delta_r \cos\psi_q \end{aligned} \tag{7}$$

where q denotes the qth rolling element; B is the inner and outer groove curvature constant; α_0 denotes the initial contact

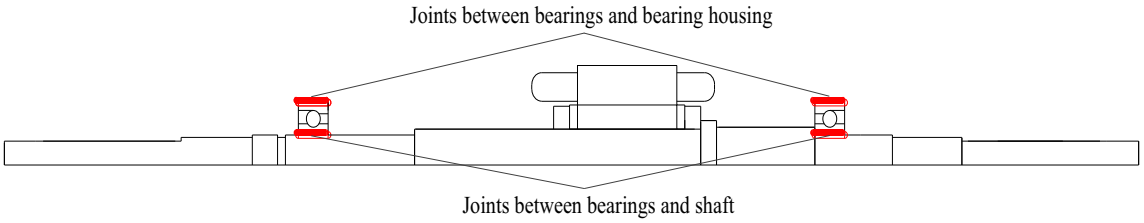

Fig. 3 Joints formed by bearings/bearing housing and bearings/shaft

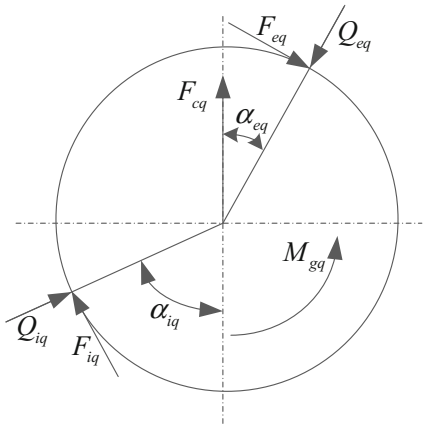

Fig. 4 Force diagram for rolling element

angle; ψ_q is the position angle of the qth rolling element; δ_a and δ_r denote the axial and radial deformations, respectively; A_{xq} and A_{zq} are the x and z coordinates of the inner and the outer groove curvature centers, respectively; θ is the angular displacement of the inner ring; and D_w is the diameter of rolling elements.

The deformation of the rolling elements and outer rings can be obtained according to the Pythagorean theorem and the geometric relationship shown in Fig. 5

$$\begin{aligned}\delta_{iq} &= \left(V_{xq}^2 + V_{zq}^2\right)^{1/2} - (f_i - 0.5)D_w \\ \delta_{eq} &= \left[\left(A_{xq} - V_{zq}\right)^2 + \left(A_{zq} - V_{zq}\right)^2\right]^{1/2} - (f_e - 0.5)D_w\end{aligned} \tag{8}$$

where δ_{iq} and δ_{eq} denote the contact deformations of the balls and rings, respectively; f_i and f_e are the curvature radius coefficients of the inner and outer grooves, respectively; and i and e denote the inner and outer rings, respectively.

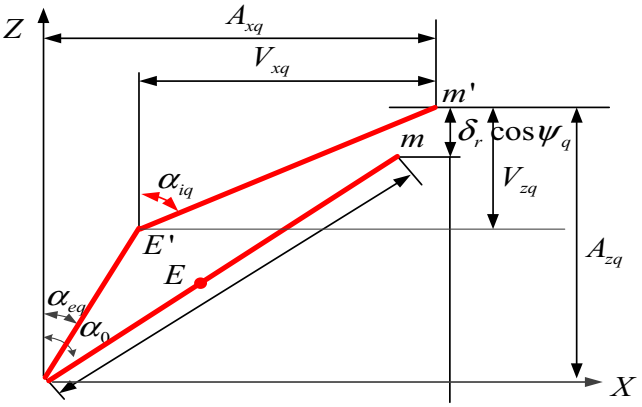

Fig. 5 Relative position between curvature centers of rolling elements and inner groove

The balance equations of rolling elements under the combined effect of loads can be expressed as

$$\begin{aligned}Q_{iq}\sin\alpha_{iq} - Q_{eq}\sin\alpha_{eq} - \frac{M_{gq}}{D_w}\left(\lambda_{iq}\cos\alpha_{iq} - \lambda_{eq}\cos\alpha_{eq}\right) &= 0 \\ Q_{iq}\cos\alpha_{iq} - Q_{eq}\cos\alpha_{eq} - \frac{M_{gq}}{D_w}\left(\lambda_{iq}\sin\alpha_{iq} - \lambda_{eq}\sin\alpha_{eq}\right) + F_{cq} &= 0\end{aligned} \tag{9}$$

where Q_{iq} and Q_{eq} are the normal loads of the qth rolling element and inner with outer rings, respectively; λ_{iq} and λ_{eq} denote the control parameters of the inner and outer ring grooves, respectively; M_{gq} and F_{cq} are the gyroscopic moment and centrifugal force of the qth rolling element, respectively; and α_{iq} and α_{eq} denote the contact angles of the rolling elements and the inner and outer rings, respectively.

The balance equations of rings can be obtained according to the balance relationships among the axial, radial, and external bending moments [13].

$$\begin{aligned}F_a - \sum_{q=1}^{Z}\left[Q_{iq}\sin\alpha_{iq} - \frac{M_{gq}}{D_w}\lambda_{iq}\cos\alpha_{iq}\right] &= 0 \\ F_r - \sum_{q=1}^{Z}\left[Q_{iq}\cos\alpha_{iq} + \frac{M_{gq}}{D_w}\lambda_{iq}\sin\alpha_{iq}\right]\cos\alpha_{iq} &= 0 \\ M - \sum_{q=1}^{Z}\left[\left(Q_{iq}\sin\alpha_{iq} - \lambda_{iq}M_{gq}\cos\alpha_{iq}\right)R_i + \lambda_{iq}r_i\frac{M_{gq}}{D_w}\right]\cos\psi_q &= 0\end{aligned} \tag{10}$$

where F_a and F_r are the radial and axial loads of the bearing, respectively; M is the external bending moment; R_i is the radius of the inner groove curvature center; and r_i is the radius of the groove.

For each ball, the force-deformation equation can be expressed as [13]

$$Q_{jq} = k_{jq}\delta_{jq}^{1.5}, (j = i, e) \tag{11}$$

where k_{jq} denotes the contact stiffness between the rolling elements and raceways.

Heat generation of high-speed angular contact ball bearing can be expressed as [14]

$$Q = \frac{2\pi}{60}nM \tag{12}$$

where Q and M denote the heat generation and friction torque of bearings, respectively, and n denotes the bearing's rotational speed.

Bearing friction moments M consists of two parts, namely, the load term M_l and speed term M_v [14]

$$M = M_l + M_v \tag{13}$$

Friction torque M_l caused by the external load can be expressed as

$$M_l = f_1 \cdot F_\beta \cdot d_m \tag{14}$$

where f_1 denotes the coefficient related to the bearing structure, d_m denotes the bearing's pitch diameter, α is the contact angle of the bearing under load, and F_β is the equivalent load applied to bearings and $F_\beta = \max(0.9F_a/\tan\alpha - 0.1F_r, F_r)$, F_a and F_r denote bearing's axial and radial loads, respectively.

The friction torque M_v caused by lubricant viscous friction can be expressed as [14]

$$\begin{cases} M_v = 10^{-7} \cdot f_o \cdot (v_o n)^{2/3} \cdot d_m^3 & \text{if } v_o n \geq 2000 \\ M_v = 160 \times 10^{-7} \cdot f_o \cdot d_m^3 & \text{if } v_o n < 2000 \end{cases} \tag{15}$$

where v_o is the lubricant's kinematic viscosity of operating temperature and f_o is related to bearing type and lubrication.

Then, the heat generation and stiffness of bearings can be calculated according to the dynamic and kinematic parameters in Eqs. (7)–(11). However, the variables in Eqs. (7)–(11) coupled to each other and hence the iterative process is complex. Moreover, it is necessary to calculate the *Jacobi* matrix when the Newton-Raphson algorithm is used to solve above nonlinear equations. And the elements of the Jacobi matrix are the partial derivatives of each equation. To prevent the nonconvergence and oscillation problems in the calculation process, relaxation factors should be introduced. Then, the dynamic and kinematic parameters required for the calculation of heat generation and stiffness can be obtained. Figure 6 depicts the algorithm of heat generation and stiffness of rolling bearing. The inputs of the algorithm are the geometry and operating parameters of bearings. And bearing geometry parameters include the basic structure and material parameters of bearings, such as the diameters of the inner and outer rings, the number and diameter of rolling elements, the curvature radius coefficients of the inner and outer grooves, the initial contact angle, and material properties (Young's modulus and Poisson's ratio, etc.).

The relationships of heat generation with the preload and speed of bearing SKF7005 ACD/P4A is shown in Fig. 7. It can be seen that the heat generation of bearings increases with the rotational speed and preload. The reason is that the increase of preload is equivalent to the increase of the external load. When the rotational speed increases, the centrifugal force and gyroscopic moment applied to rolling elements increase as well, resulting in an increase in the friction between rolling elements and the rings and hence bearing's heat generation increases.

Fig. 6 Calculation process of quasi-statics of high-speed ball bearing

3.3 Heat dissipation

The convective heat transfer coefficient can be expressed as [15]

$$\alpha = \frac{\mathrm{Nu} \cdot \lambda_{\mathrm{fluid}}}{d_h} \tag{16}$$

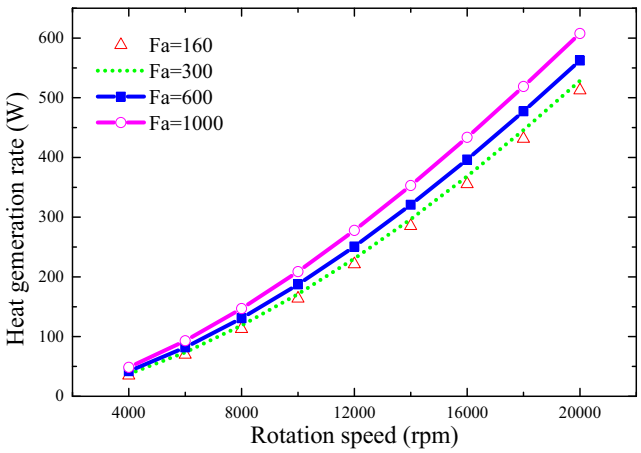

Fig. 7 Relationship between heat generation and preload, speed

where d_h denotes the hydraulic diameter, λ_{fluid} is the fluid's thermal conductivity, and Nu denotes the Nusselt number.

The heat transfer mode of moving components belongs to forced convection, such as the convective modes between the stator and cooling water, stator and rotor, shaft and air. While the heat transfer mode of stationary components belongs to free convection, such as the convective between the spindle housing and air. Then, Nusselt number Nu can be calculated based on different convection heat transfer models listed in Table 2.

Where Pr is the Prandtl number, Re is the Reynolds number, l_t is the length of water tube, w is the velocity of the water, η denotes the fluid's kinematic viscosity, d_k is the loop diameter, d_s is the diameter of the headstock, g is the earth gravity, and ξ denotes the friction factor and its value is $\xi=1/[0.79\ \ln(\text{Re})-1.64]^2$.

3.4 Modeling thermal contact resistance

All the surfaces are rough when viewed microscopically. Namely, the surface is composed of numerous asperities with different scales, and hence, the contact of two surfaces happens at finite discrete points. When the heat flows through the imperfect contact of two contacting surfaces, heat flux may contract at these contacting points, as shown in Fig. 8. On the other hand, the imperfect contact produced by surface roughness indicates that there are many contact points and cavities at the contact interface, as shown in Fig. 9. Generally, the thermal conductivity of the filling material in the cavities (such as air or oil) is much lower than that of the parts, and hence, the TCR and temperature jumps are formed at the joint surface. Namely, TCR plays the role of restricting the heat flowing from the heat source to another object contacting with the heat source, which results in a high local temperature of the heat source.

The TCR model developed by Mikic, which assumed that all the contacts are under elastic deformation, was unreasonable [19]. Yovanovich also proposed a TCR model which assumed that all the contacts are under plastic deformation [20]. In fact, elastic, elastic-plastic, and plastic deformations occur on contact interface. Moreover, the most traditional research methods on TCR were based on statistical theory and experiments [21–23]. However, the method based on the statistical theory was sensitive to the sampling length and resolution of the instrument [21, 22], and the method based on experiments had its own disadvantages, such as the poor generality, worse adaptability, and some uncertainties [22, 23]. When any one among such factors as material, mean roughness, and the contact pressure change, the experiment has to be redesigned. On the other hand, it is difficult to predict TCR because the strongly nonlinear relationship between TCR and many other factors, such as surface morphology, interface pressure, contact deformation modes, contact area, material properties, and temperature, among which the surface morphology is a major determinant. TCR is a complex interdisciplinary problem, including geometry, mechanical, and thermal subproblems. And the core of TCR model is its geometry and mechanical issues. Therefore, it is essential to propose a geometrical-mechanical-thermal predictive model to overcome the shortages of traditional TCR models.

3.4.1 Characterization of rough surfaces

The Weierstrass-Mandelbrot function (W-M) in fractal geometry is the most commonly used function to characterize the rough morphology of bearing rings with disorder, nonstationary random, and self-affinity features [24].

$$z(x) = G^{(D-1)}\sum_{n=n_1}^{\infty}\frac{\cos 2\pi\gamma^n}{\gamma^{(2-D)n}};\ 1<D<2;\ \gamma>1 \tag{17}$$

where $z(x)$ and x denote the profile height function and measuring position; D (dimensionless parameter) is the fractal dimension of the profile of the surface, varying from 1 to 2; G is a scaling constant and is not limited to a specific range

Table 2 Calculation of Nusselt number

Convective boundary condition	Characteristic size	Convection model
Forced convection of the annular gap [16]	d_h	$\text{Nu}=0.133\text{Re}^{2/3}\cdot\text{Pr}^{1/3}$ $\text{Re}<4.3\times10^5, 0.7<\text{Pr}<670$
Spindle housing outer surface free convection heat transfer [17]	d_h	$\text{Nu}=\left\{\frac{0.125\xi(\text{Re}-1000)\text{Pr}}{1+12.7\sqrt{0.125\xi\left(\text{Pr}^{2/3}-1\right)}}\left[1+(d_h/l_t)^{2/3}\right]\right\}\left[1+3.6(1-d_h/d_k)(d_h/d_k)^{0.8}\right]$ $\text{Re}=wd_h/\eta, 2\times10^4\le\text{Re}\le1.5\times10^5, 5\le d_h/d_k\le84$
Forced convection of the cooling system and stator [18]	l	$\text{Nu}=0.133\text{Re}^{0.8}\text{Pr}^{0.3}$ $\text{Re}>10000, 0.7<\text{Pr}<100, L/h_{\text{gap}}>60$

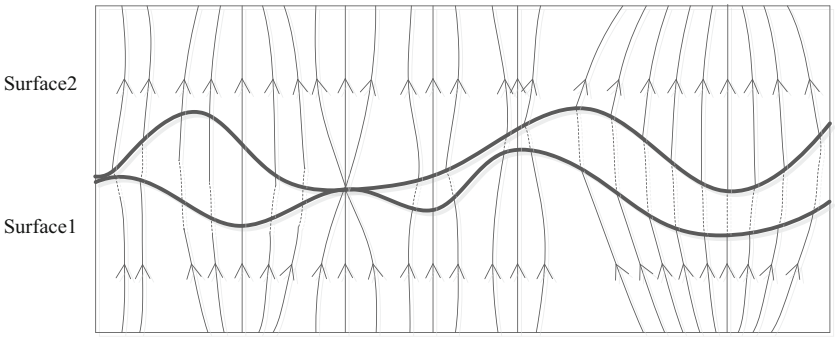

Fig. 8 Constriction of heat flow lines through contacting spots

and has a length dimension, the frequency expression is $\omega=\gamma^n$; and γ is related to the sampling length L ($\gamma^{n_1}\approx 1/L$, n_1 corresponding to the low cutoff frequency of the profile).

The power spectrum of the W-M function is given by Majumdar and Tien [25]

$$S(\omega)=\frac{G^{2(D-1)}}{2\ln\gamma}\frac{1}{\omega^{(5-2D)}} \tag{18}$$

The W-M function also follows the relationship

$$z(\gamma x)=\gamma^{(2-D)}z(x) \tag{19}$$

It is obvious to find that two scale-invariant parameters G and D are scale independent and that W-M function is a self-similar function, which is not sensitive to the sampling length and resolution of the measuring instrument. Therefore, the W-M function can be applied to characterize the surface morphology of bearing rings. Figure 10 illustrates a 3D fractal surface morphology and its contour plane generated from Eq. (17) with D=1. 64, G=9.46e–6 m, L=1 μm, and γ=1.5.

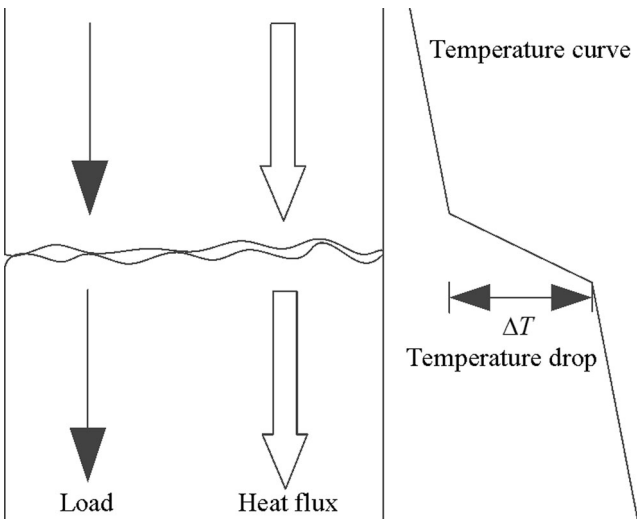

Fig. 9 Temperature drop at the contact interface

3.4.2 Fractal parameters identification

In order to identify the fractal parameters, the surface morphology of bearing rings is measured by an Olympus laser microscope. Assuming that the sampling interval is Δt and the total number of the samples is N, then, the profile height can be written as

$$z(x_i)=z_i(i=0,1,2,\ldots,N-1) \tag{20}$$

Assuming that $\tau=n\Delta t$, then the structure function of bearing ring's rough surface morphology can be expressed as

$$s(\tau)=\left\langle[z(x+\tau)-z(x)]^2\right\rangle=\int_{-\infty}^{+\infty}S(\omega)\left(e^{j\omega\tau}-1\right) \quad (21-\text{a})$$

Substituting Eq. (18) into Eq. (21-a), the following relationship can be obtained

$$s(\tau)=CG^{2(D-1)}\tau^{(4-2D)}=\frac{1}{N-n}\sum_{i=0}^{N-n-1}(z_{i+n}-z_i)^2 \quad (21-\text{b})$$

where C denotes a constant and $C=\Gamma(2D-3)\frac{\sin[(D-1.5)\pi]}{(4-2D)}\ln\gamma$.

Equation (21-b) is taken logarithm on both sides, then

$$\log S(\tau)=\log C+2(D-1)\log G+(4-2D)\log\tau \quad (21-\text{c})$$

Assuming that $k=4-2D$, $b=\log C+2(D-1)\log G$, then Eq. (21-c) can be written as

$$\lg S(\tau)=k\lg\tau+b \quad (21-\text{d})$$

It can be seen from Eq. (21-d) that the structure function is close to a linear function in the double logarithmic coordinates, the fractal dimension D can be obtained from the slope

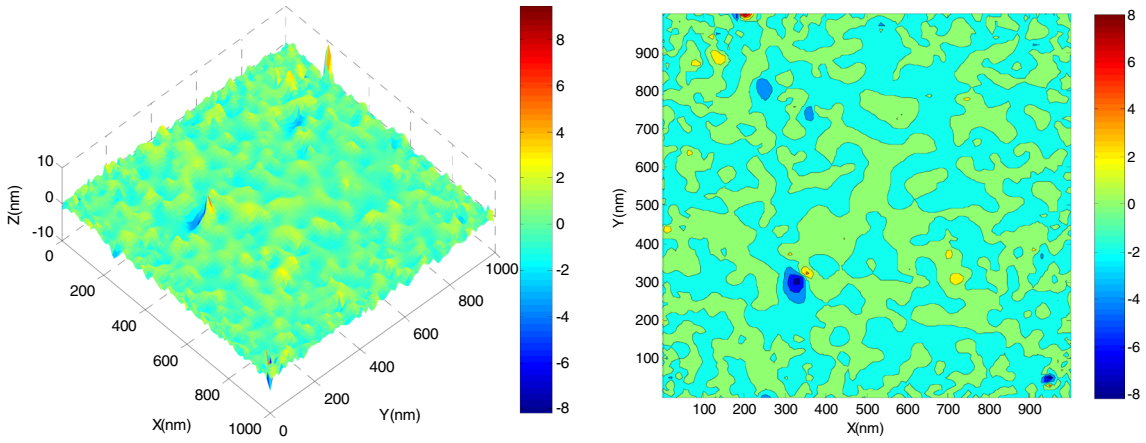

Fig. 10 A 3D fractal surface morphology generated by W-M function: **a** micromorphology, **b** contour plane

of the line, and the scaling constant G can be obtained by the intersection with the longitudinal axis.

Namely,

$$\left\{\begin{array}{l} D=\dfrac{(4-k)}{2} \\ \log G=\dfrac{b-\log C}{2(D-1)} \end{array}\right\} \tag{22}$$

3.4.3 Contact mechanics model of asperities

If the smaller scale terms are ignored and the first term of the W-M function is taken, the profile of rough surfaces can be obtained in the range of l, as shown in Fig. 11.

$$z(x)=G^{D-1}l^{2-D}\cos\frac{\pi x}{l} \quad \left(-l/2<x<l/2\right) \tag{23}$$

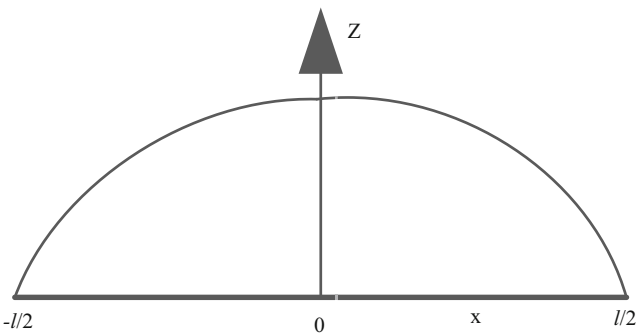

Fig. 11 Geometry of a contact spot of length scale l

Then, the asperity top radius can be expressed as [26]

$$R=\left|1\Big/\left|\frac{d^2z}{dx^2}\right|_{x=0}\right|=\frac{a^{D/2}}{\pi^2G^{D-1}} \tag{24}$$

If the maximum area of contacts is a_L, then the number of the asperities whose area is larger than a can be expressed as [26]

$$N(A>a)=\left(\frac{a_L}{a}\right)^{D/2} \tag{25}$$

The number of the asperities whose area is between a and $a+da$ can be expressed as

$$n(a)=-\frac{dN}{da}=\frac{D}{2}\frac{a_L^{D/2}}{a^{\left(D/2+1\right)}} \tag{26}$$

In order to determine the contact parameters of the asperities, it is essential to investigate the contact states of the asperities, namely, three modes of elastic, elastic-plastic, and plastic deformations should be considered. When the maximum of Hertz pressure applied to the asperities reaches $0.6H$, plastic flow begins to occur on the contacting asperities. And the critical plastic contact area a_{cl} corresponding to the beginning of plastic deformation can be obtained [27]

$$a_{c1}=G^2\Big/\left(\frac{0.6H}{2E}\right)^{2/(D-1)} \tag{27}$$

where H denotes the microhardness of the softer material, and E denotes the equivalent elastic modulus, namely,

$$\frac{1}{E}=\frac{1-v_1^2}{E_1}+\frac{1-v_2^2}{E_2} \tag{28}$$

where subscripts 1 and 2 refer to the two contacting surfaces; and E_1, E_2, v_1, and v_2 denote Young's elastic modulus and Poisson's ratio of the two contacting materials, respectively.

When the minimum of contact pressure applied to the asperities reaches H, fully plastic flow occurs on the surface. Then, the critical contact area a_{c2} corresponding to the fully plastic deformation can be expressed as

$$a_{c2}=G^2\Big/\left(\frac{3H}{4E}\right)^{2\Big/(D-1)} \tag{29}$$

(1) Elastic contact.

When the normal deformation ε is small enough, namely, $a<a_{c1}$ is satisfied, elastic deformation occurs on the contacting asperities. And the deformation rule of asperities is in compliance with the Hertz elastic contact theory. Therefore, when the asperities are in contact with a rigid and smooth plane, the actual contact area a_{ce}, the average contact pressure P_{ce}, and the load $F_{ce}(\varepsilon)$ on each contacting asperity can be obtained according to Greenwood et al. [21]

$$a_{ce}=\pi R\varepsilon \tag{30-a}$$

$$P_{ce}=\frac{4E}{3\pi}\left(\frac{\varepsilon}{R}\right)^{\frac{1}{2}} \tag{30-b}$$

$$F_{ce}(\varepsilon)=\frac{4}{3}ER^{\frac{1}{2}}\varepsilon^{\frac{3}{2}} \tag{30-c}$$

By eliminating the normal deformation ε, the relationship between $F_{ce}(\varepsilon)$ and the contact area can be obtained

$$F_{ce}(\varepsilon)=\frac{4Ea'^{\frac{3}{2}}}{3\pi^{\frac{3}{2}}R} \tag{30-d}$$

where the contact area is half of the geometric cross-sectional area, namely, $a'=a/2$.

(2) Elastic-plastic contact.

When the deformation ε of the asperity is moderate, namely, $a_{c1}\le a\le a_{c2}$ is satisfied, elastic and plastic deformations occur on the contact interface. According to the continuous and smooth nature in the mathematical sense, a template function is developed as

$$f(\varepsilon)=-2\left(\frac{\varepsilon-\varepsilon_{c1}}{\varepsilon_{c2}-\varepsilon_{c1}}\right)^3+3\left(\frac{\varepsilon-\varepsilon_{c1}}{\varepsilon_{c2}-\varepsilon_{c1}}\right)^2 \tag{31-a}$$

where

$$\begin{aligned}\varepsilon_{c1}&=\left(kH\Big/(2E)\right)^2\cdot a^{D\Big/2}\Big/G^{D-1}\\ \varepsilon_{c2}&=\left(3H\pi\Big/(4E)\right)^2\cdot R\end{aligned} \tag{31-b}$$

The actual contact area a_{cep}, the average contact pressure P_{cep}, and the load $F_{\mathrm{cep}}(\varepsilon)$ on each contacting asperity can be expressed as

$$a_{\mathrm{cep}}=\pi R\varepsilon[1+f(\varepsilon)] \tag{31-c}$$

$$P_{\mathrm{cep}}=kH\left(\varepsilon\Big/\varepsilon_{c1}\right)^{1\Big/2}+\left[H-kH\left(\varepsilon\Big/\varepsilon_{c1}\right)^{1\Big/2}\right]f(\varepsilon) \tag{31-d}$$

$$\begin{aligned}F_{\mathrm{cep}}&=a_{\mathrm{ep}}P_{\mathrm{ep}}\\&=\pi R\varepsilon[1+f(\varepsilon)]\left\{kH\left(\varepsilon\Big/\varepsilon_{c1}\right)^{1\Big/2}+\left[H-kH\left(\varepsilon\Big/\varepsilon_{c1}\right)^{1\Big/2}\right]f(\varepsilon)\right\}\end{aligned} \tag{31-e}$$

(3) Fully plastic contact

When the deformation ε of the asperity is relatively large, namely, $a>a_{c2}$ is satisfied, fully plastic deformation occurs on the contacting asperities. The contact pressure P_{cp}, contact area a_{cp} of each asperity, and the load F_{cp} on each contacting asperity can be obtained

according to Cooper et al. [22]

$$a_{cp} = 2\pi R\varepsilon \tag{32 – a}$$

$$P_{cp} = H \tag{32 – b}$$

$$F_{cp} = Ha \tag{32 – c}$$

The total actual area A_r can be calculated

$$A_r = \int_0^{a_L} n(a)ada = \frac{D}{4-2D}\left(a_L + a_L^{D/2}\, a_{c1}^{(2-D)/2}\right) \tag{33}$$

Through above analysis, the load on each contacting asperity and the actual contact area can be obtained. Then, the load distribution on the entire contact interface can be obtained by integrating surface loads from 0 to a_L. When the fractal dimension $D \neq 1.5$, the load on the joint surface can be divided into three cases.

If $a_L < a_{c2}$, then

$$F = HA_r. \tag{34 – a}$$

If $a_{c2} < a < a_{c1}$, then

$$F = H\frac{D}{2-D}a_L^{D/2}\, a_{c2}^{(2-D)/2} + \int_{a_{c2}}^{a_L} n(a)g_2\left[g_1^{-1}(a)\right]da \tag{34 – b}$$

$$\text{where } \begin{cases} g_1(a) = \dfrac{a}{3-2a}\left(\dfrac{2-a}{a}\right)^{a/2} \\ g_2(a) = \left(\dfrac{a}{2-a}\right)^{(2-a)/2} \end{cases}$$

If $a > a_{c1}$, then

$$F = H\frac{D}{2-D}a_L^{D/2}\, a_{c2}^{(2-D)/2} + \int_{a_{c2}}^{a_{c1}} n(a)g_2\left[g_1^{-1}(a)\right]da + \frac{4\sqrt{\pi}}{3}EG^{(D-1)}\frac{D}{(3-2D)}2^{(D-3)/2}a_L^{D/2}\left(a_L^{(3-2D)/2} - a_{c1}^{(3-2D)/2}\right) \tag{34 – c}$$

When the fractal dimension $D=1.5$, the load on the joint surface can be expressed as

$$F = 3Ha_L^{3/4}a_{c2}^{1/4} + \int_{a_{c2}}^{a_{c1}} n(a)g_2\left[g_1^{-1}(a)\right]da + \sqrt{\pi}EG^{1/2}\left(\frac{a_L}{2}\right)^{3/4}\ln\left(\frac{a_L}{a_{c1}}\right) \tag{34 – d}$$

The dimensionless parameters are defined as

$$F^* = \frac{F}{A_aE}; A_r^* = \frac{A_r}{A_a} \tag{35}$$

The maximum area a_L of contacts can be obtained by applying Eq. (34) under a certain external load F_{ext} which should be equal to the load F on the joint surface. And the total actual contact area can be obtained according to Eq. (33). Moreover, the fractal parameters G and D are identified by the structure function method, as shown in Section 3.4.2. Besides, the relationship between the dimensionless load F^* and actual contact area A_r^* can be obtained by Eq. (35).

3.4.4 Modeling thermal contact resistance

It can be seen from the above analysis that the contact of two contacting surfaces occurs at finite discrete points; each contact forms a microthermal resistance. Besides, contraction thermal resistance at the contact interface should also be taken into account. Due to the self-similar characteristics of rough surfaces, all of these microthermal resistances form a thermal network in series and parallel. The network of fractal TCR is shown in Fig. 12. The total TCR R_t can be expressed as [25]

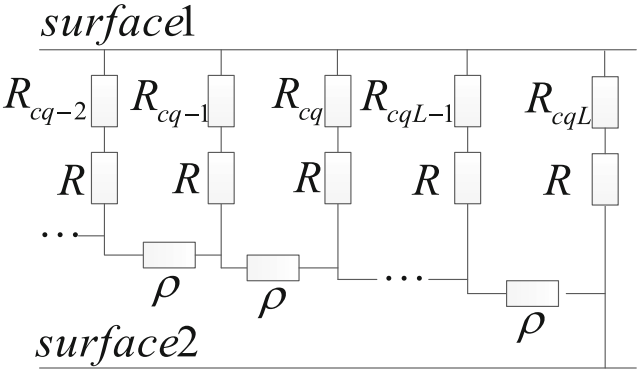

Fig. 12 Total fractal thermal resistance network

$$\frac{1}{R_t}=\frac{1}{R+R_{cq_L}}+\frac{1}{\rho+\dfrac{1}{R+R_{cq_L+1}+\dfrac{1}{\rho+\dfrac{1}{R+R_{cq_L+2}+\dfrac{1}{\rho+\cdots}}}}}\tag{36}$$

where R denotes the equivalent thermal resistance of all series and parallel bulk resistances of the qth contacting point and it can be expressed as [25]

$$R=\frac{G^{D-1}}{k_sL^D}\left[\left(\frac{D}{2-D}\right)\frac{1}{A_r^*}\right]^{\frac{1}{2}}\left[1-1\Big/\left(1+\left(\frac{1-A_r^*}{A_r^*}\right)^{\frac{1}{2}}\right)\right]\tag{37}$$

where L is the nominal size of the contact interface, A_r^* is the dimensionless actual contact area (contact ratio), and R_{cq} denotes the equivalent contraction thermal resistance of the q contact points, and ρ denotes the equivalent thermal resistance of all parallel thermal resistance and it can be expressed as [25]

$$\rho=\frac{G^{D-1}}{k_sL^D}\left[\left(\frac{D}{2-D}\right)\frac{1}{A_r^*}\right]\tag{38}$$

k_s is the equivalent thermal conductivity determined by

$$\frac{2}{k_s}=\frac{1}{k_1}+\frac{1}{k_2}\tag{39}$$

where k_1 and k_2 denote the thermal conductivity of the two contacting materials, respectively.

A single microcontact between two rough surfaces is schematically illustrated in Fig. 13. Heat flux contracts at the contact interface because the imperfect contact of two contacting surfaces. According to Cooper et al. [22], thermal contraction resistance of a contact can be expressed as

$$r_c=\frac{1}{2ck_s}\phi\left(c\Big/b\right)\tag{40}$$

where ϕ is the interface contraction ratio and can be approximately expressed by

$$\phi\left(c\Big/b\right)=\left(1-c\Big/b\right)^{1.5}\tag{41}$$

where b and c, which can be calculated by applying Eq. (42), are the radii of the contact area and the heat flow channel, respectively.

$$c\Big/b=\left(A_r^*\right)^{1\Big/2}\tag{42}$$

Since the relationship of the thermal contraction resistances among the q contact points is parallel, the equivalent thermal contraction resistance of the q contact points can be expressed as

$$R_{cq}=\frac{1}{2k_sL^D}\left[\frac{D}{(2-D)A_r^*}\right]\left[1-\left(1\Big/\left(1+\left(\frac{1-A_r^*}{A_r^*}\right)^{\frac{1}{2}}\right)\right)\right]^{1.5}a_q^{(D-1)\Big/2}\tag{43}$$

where $a_q=A_a/b^{2q}$, b is a real number greater than 1, the variation range of q is $q_L<q<\infty$, q_L corresponds to the maximum point of contact, and q_L satisfies the following relationship [25]

$$b^{q_L}=\left[\left(\frac{D}{2-D}\right)\frac{1}{A_r^*}\right]^{1\Big/2}\tag{44}$$

where $R_{cq_{L+i}}(i=0\sim\infty)$ denotes the thermal contraction resistance of a group contacts with the same area.

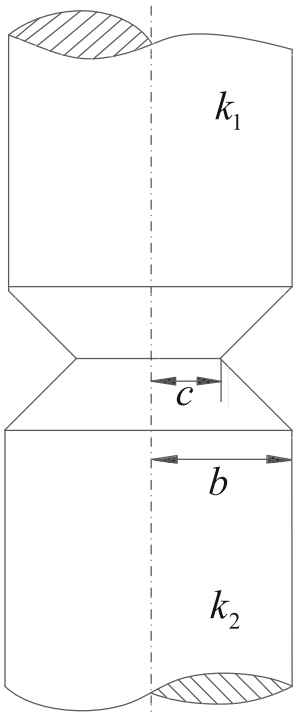

Fig. 13 Schematic diagram of a microcontact spot

Substituting Eqs. (37), (38), (39), and (43) into Eq. (36), the total thermal contact resistance R_t can be obtained. The simplified expression of thermal contact conductance h can be expressed as

$$h = k_s L^D \left[\frac{2-D}{D} A_r^*\right]^{D/2} f\left(G, D, L, A_r^*\right) \tag{45}$$

Then, the thermal contact resistance R can be obtained

$$R = \frac{1}{h} \tag{46}$$

3.5 Bearing stiffness

Bearing's axial and radial stiffness have great effect on the thermal deformation of the high-speed spindle system. Therefore, it is essential to know the axial and radial stiffness of the bearing when calculating the deformation of the high-speed spindle. The bearing stiffness can be obtained according to the rolling bearing quasi-static mechanics analysis. The relationship between bearing stiffness and preload is shown in Fig. 14.

4 Model validation

4.1 Experimental setup

The experimental setup is a high-speed spindle system, as shown in Fig. 15. The measuring equipment and functions are as follows: a synchronous acquisition system developed by our group with American NI-SCXI 1600 as its structural base was used to determine the temperature and thermal deformation. This system used PT100 precision magnetic

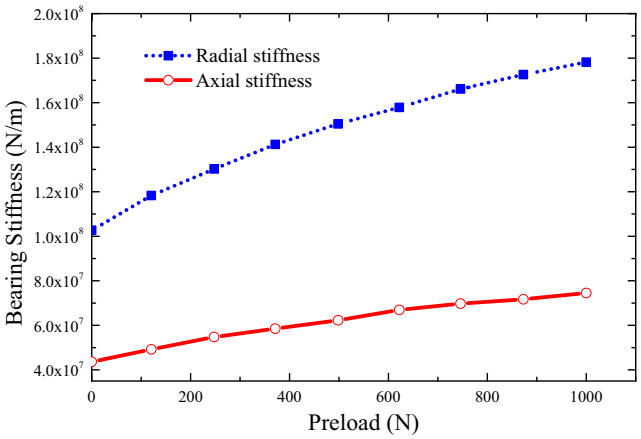

Fig. 14 Relationship between bearing stiffness and preload

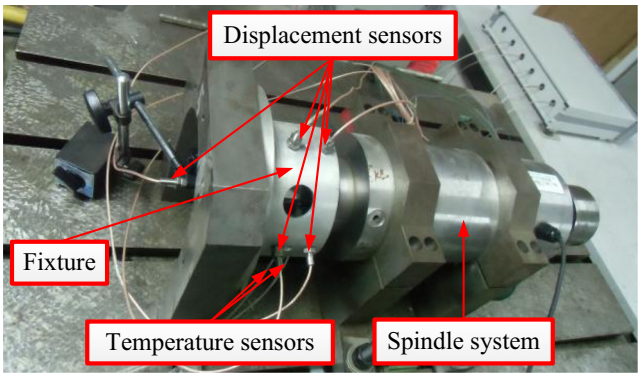

Fig. 15 Experimental setup

temperature sensors to measure the temperatures of the bearings, motor, water jacket, spindle housing, and ambient. High-precision eddy-current sensors were applied to collect the spindle thermal drifts. And the temperatures and thermal drifts are monitored in the experiments every 1 s [28]. The rough morphology of bearing surface was measured by an Olympus laser microscope LEXT OLS4000, as shown in Fig. 16.

4.2 Measuring principles

The system carries out real-time synchronous acquisition of temperatures and thermal drifts. The mounting positions of the magnetic temperature sensors (PT100) are as follows: front bearing (T_1), rear bearing (T_2), stator (T_3), cooling jacket (T_4), ambient (T_5), and spindle housing (T_6). The mounting positions of the eddy-current displacement sensors are as follows: radial distal Z-axis (S_1), radial distal X-axis (S_2), radial near Z-axis (S_3), radial near X-axis (S_4), and Y axial-direction (S_5), as shown in Figs. 15 and 17. The spindle thermal drifts are measured by using the five-point method [28].

The rotational speed distribution of the spindle is 15, 000 rpm, as shown in Fig. 18, and the spindle runs 4 h till it reaches a thermal equilibrium state and then stops for 2 h [28].

The spindle is parallel to the Y-axis, and the axial thermal expansion can be obtained by the displacement sensor S5. The radial thermal yaw θ_x partial X-direction is measured by the S_1

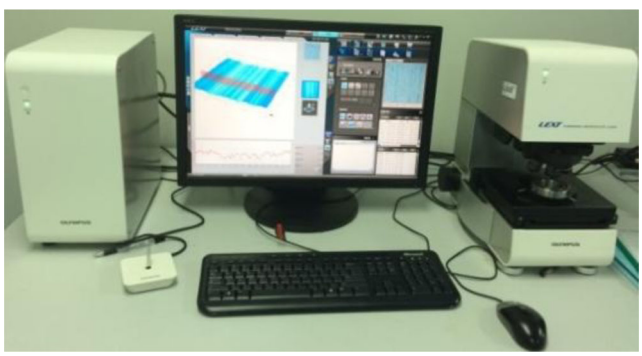

Fig. 16 Olympus LEXT OLS4000 laser microscope

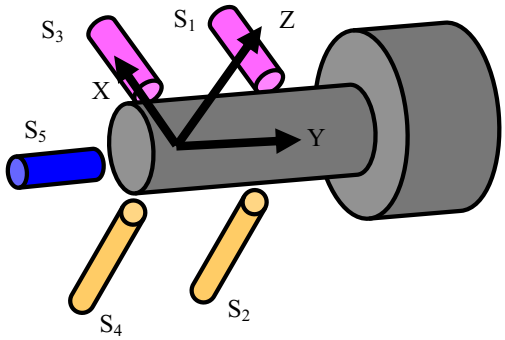

Fig. 17 Spindle five-spot installation diagram

and S_3, and the radial thermal pitch θ_y partial Z-direction is measured by the S_2 and S_4, as shown in Fig. 19.

Then, the thermal yaw and thermal pitch angles can be calculated [28]. It can be seen from Fig. 19 that the thermal yaw angle can be expressed as Eq. (47)

$$\theta_x = \frac{(L_3{}^i - L_1{}^i) - (L_3{}^0 - L_1{}^0)}{D} \tag{47}$$

where $L_3{}^0$ and $L_1{}^0$ are the radial displacements between the sensor probes and the spindle measured by S_3 and S_1, respectively, in the initial state, and $L_3{}^i$ and $L_1{}^i$ are the transient displacements during the running operation. D is the distance between S_1 and S_3, and D=120 mm.

Similarly, the thermal pitch angle in the Z-direction can be obtained

$$\theta_y = \frac{(L_4{}^i - L_2{}^i) - (L_4{}^0 - L_2{}^0)}{D} \tag{48}$$

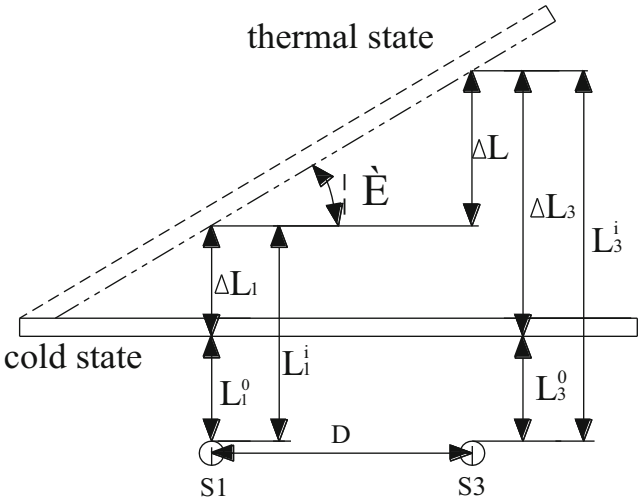

Fig. 19 The spindle thermal inclination sketch

4.3 Identification of fractal parameters

The fractal parameters G and D can then be obtained from the experimental data and Eq. (22) by means of curve-fitting. The 3D rough morphology of bearing rings was measured by the Olympus laser microscope LEXT OLS4000, as shown in Fig. 20. And the profile height along the X-direction is shown in Fig. 21, and its value is the data source to identify fractal parameters G and D.

The structure function method shown in Section 3.4.2 is utilized to identify the fractal parameters. The structure function of fractal surface is calculated by combining the data shown in Fig. 21 and Eq. (21-b), as shown in Fig. 22. It can be seen that the structure function is close to a linear function in its full range. Moreover, the least square fitting is used to obtain a straight line. Then, the fractal parameters G and D can be calculated according to the slope and the intersection with

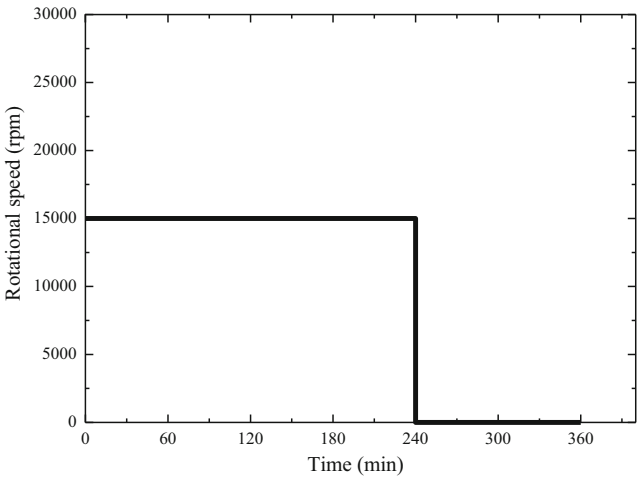

Fig. 18 Rotational speed distribution

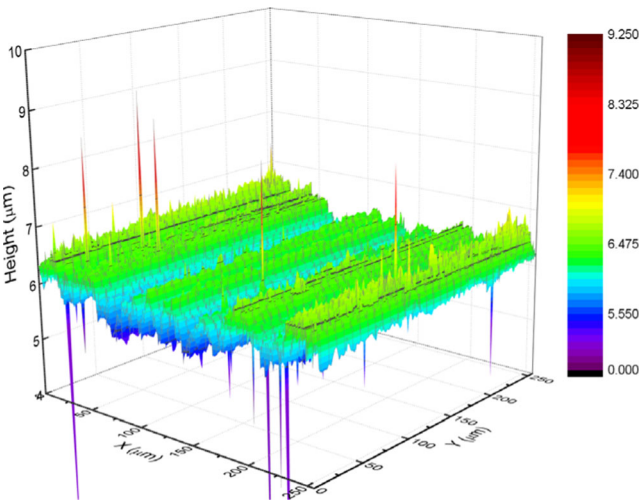

Fig. 20 3D rough morphology of bearing rings

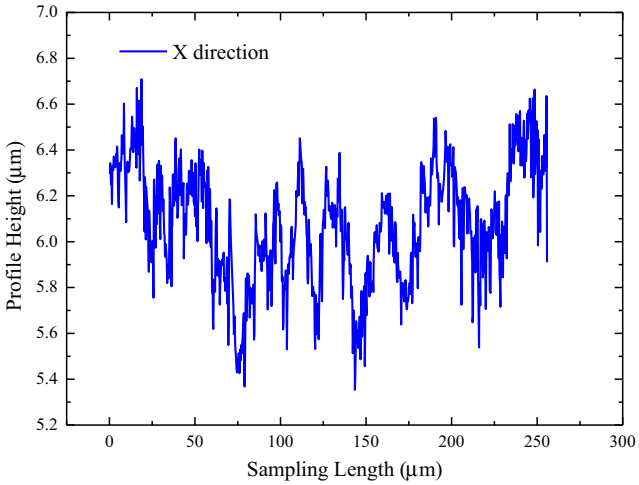

Fig. 21 Profile height of *X*-direction

the longitudinal axis of the line, which can be used as the input parameters for the modeling of TCR.

4.4 Experimental results analysis

Thermal loads, convective heat transfer coefficients, TCRs, and bearing stiffness can be obtained according to the discussion in Sections 3.2 to 3.5. When the rotational speed of the spindle is 15,000 rpm and air cutting is assumed, the heat powers of the front and rear bearings are 385 and 346 W, respectively. The heat generation for the stator and rotor are 1058 and 529 W, respectively. The convective heat transfer coefficients are as follows: stator and cooling jacket (1064.2 W/(m^2·K)), stator and rotor (146.3 W/(m^2·K)), shaft and air (86.3 W/(m^2·K)), and spindle outer housing and air (9.7 W/(m^2·K)). TCRs are as follows: bearing/bearing housing (6238 m^2·K/W) and bearing/shaft (5625 m^2·K/W). The temperature field and thermal deformation of the high-speed spindle system can be simulated by applying the above boundary conditions to the spindle thermal analysis model.

The graphs of temperature and distortion versus time during the whole spindle running period (4 h) are shown in Fig. 23. It can be seen that in 1 h, the whole spindle system reached a thermal equilibrium state. Therefore, the temperature field distribution and thermal drifts in the first 1 h are discussed.

The tilt angles, including the radial thermal yaw angle θ_x and thermal pitch angle θ_y, can be obtained according to Eqs. (47) and (48), respectively, as shown in Fig. 24.

Then, the typical presentation of results can be presented according to ISO 230-3-2007, as shown in Table 3.

where X1, Y, and Z1 denote the maximum thermal deformations of *X*, *Y*, and *Z* directions during the first 60 min and spindle running period (240 min), respectively, and A and B denote the maximum thermal tilt angles of *X* and *Z* directions during the first 60 min and spindle running period (240 min), respectively.

It can be seen that the data of the first 60 min and during the spindle running period (240 min) in Table 3 are almost the same. The reason is that the whole spindle system reached a thermal equilibrium state in 1 h. Therefore, the data of the following 3 h are almost the same.

4.4.1 Temperature field analysis

The distribution of the temperature field when the thermal equilibrium state is reached is shown in Fig. 25. It can be seen that spindle system's temperature field distribution is not uniform and the temperature gradient is obvious.

The heat generated by the front and rear bearings flows into the shaft and bearing housing. The temperature gradients of the bearing and shaft joints, bearing and bearing housing joints are obvious because the effects of TCRs make the bearings' heat dissipation condition deteriorate. Namely, the heat generated by the bearing is accumulated because the effects of TCRs, and hence the local temperature of the bearing is higher than that of the shaft and bearing housing. And the greater the

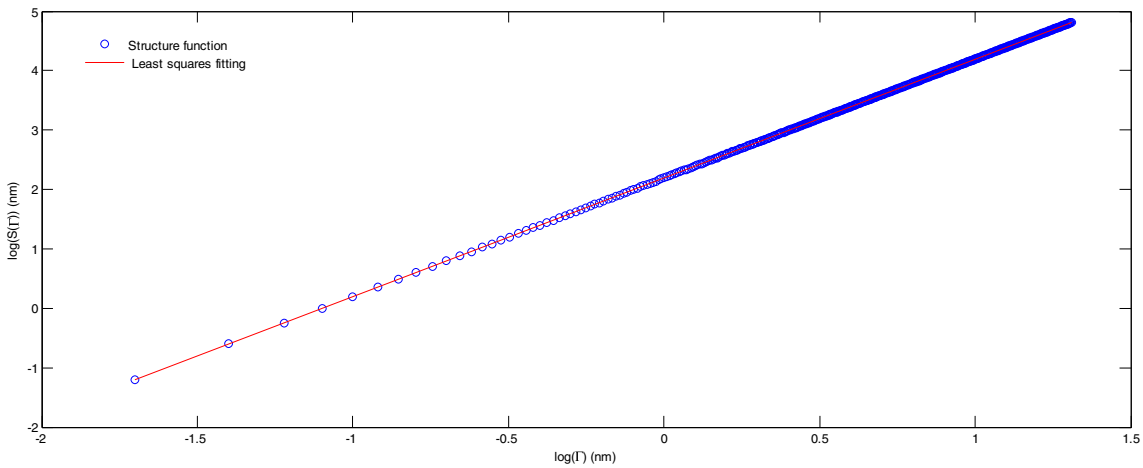

Fig. 22 Structure function in double logarithmic coordinates

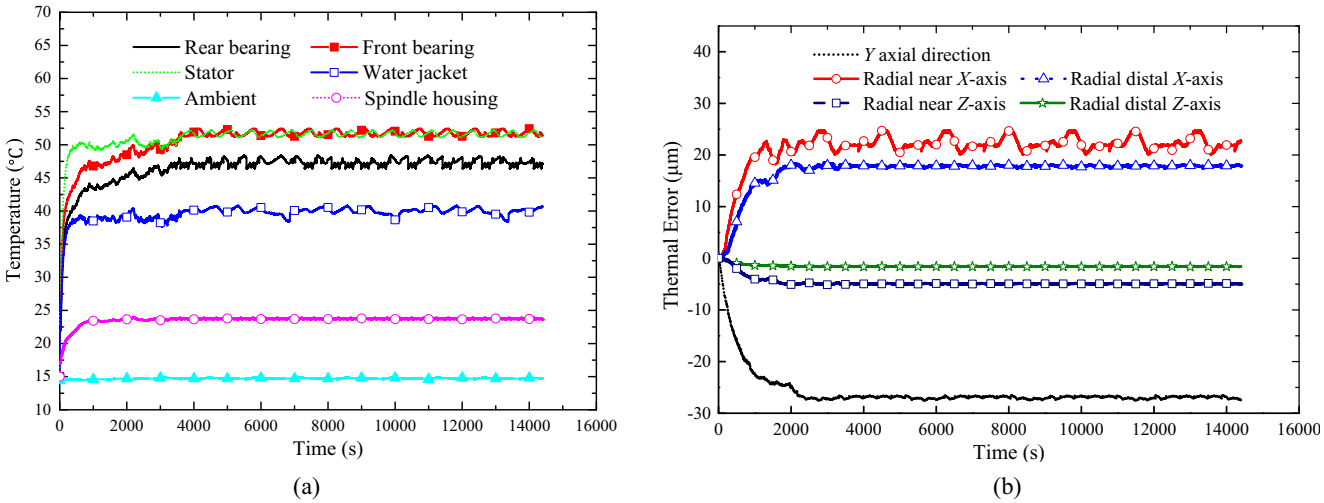

Fig. 23 Thermal characteristics of the high-speed system during total spindle running period: **a** temperature distribution, **b** thermal errors

TCRs of bearing/shaft and bearing/bearing housing are, the greater the temperature difference between the two sides of the joint surface will be.

The temperature contours of the bearings, stator, and water jacket are shown in Fig. 26. It can be seen from Fig. 26a that the temperature of the region contacting with shaft and bearing housing is lower than that of other regions because the heat of the region contacting with shaft and bearing housing flows into shaft and bearing housing. And the smaller the TCRs of bearing/shaft and bearing/bearing housing are, the lower is the temperature of the region contacting with shaft and bearing housing.

Because the front bearing is closer to the rotor than the rear bearing, the amount of the heat flowing into front bearing is more than that into the rear bearing, and hence, the temperature field distribution of front bearing is different from that of the rear bearing. Moreover, it can be seen from Fig. 26b that the temperature of the inner ring is higher than that of the outer ring because the heat generated by the rotor flows into the inner ring and the heat of the outer ring flows into the bearing housing.

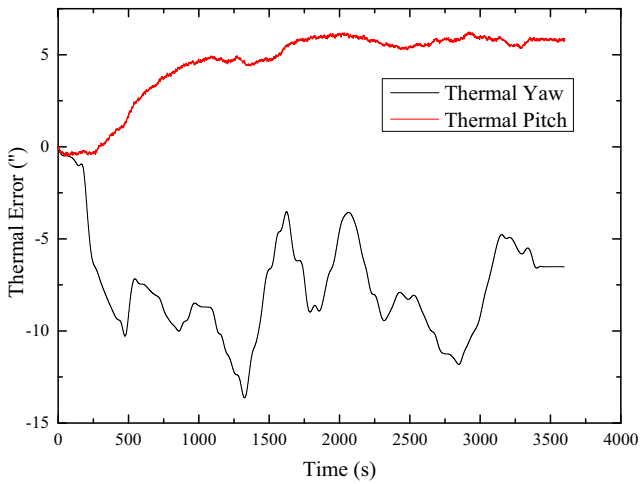

Fig. 24 Spindle thermal tilt

It can be seen from Fig. 26c that the temperature of the region contacting with the cooling jacket is lower than that of other regions because the cooling system removes most of the heat generated by the stator. And the farther away from the contacting region of stator and water jacket, the higher the temperature will be. Correspondingly, the temperature field distribution of the water jacket is contrary to that of the stator, as shown in Fig. 26d.

The maximum internal temperature of the spindle system reaches 74.5 °C (rotor). The heat generation of the stator is the max among all heat sources. However, the temperature of the stator is lower than that of the rotor because the cooling system removes most of the heat generated by the stator and the heat generated by the rotor is accumulated. And a considerable of heat generated by the stator flows into the water jacket, resulting in a rise of the temperature of the water jacket. Moreover, the temperature of the spindle housing rises up because some of the water jacket's heat flows into the spindle housing. In fact, the working mechanism of the cooling system is by sensing the temperature of cooling water outlet to control the temperature of the whole spindle system. When the cooling water's temperature is higher than the critical value, the cooling system starts to work.

Table 3 Typical presentation of results from tests of thermal distortion caused by rotating spindle

	X1 μm	Z1 μm	Y μm	A ″	B ″
During first 60 min	24.81	−5.04	−27.62	−13.64	6.26
During spindle running period t (240 min)	24.81	−5.26	−27.62	−13.64	6.26
Distance l	120 mm				

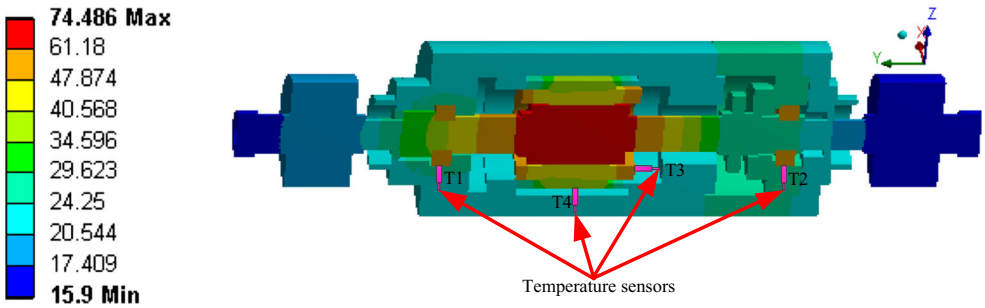

Fig. 25 Nephogram of temperature field distribution when thermal equilibrium

The mounting positions of the temperature sensors are as follows: front bearing (T1), rear bearing (T2), stator (T3), and cooling jacket (T4), as shown in Fig. 25. And the temperature data are compared with the simulated temperature histories of the corresponding positions, respectively, as shown in Fig. 27.

It can be seen that the temperature predictions of the front and rear bearings, stator, and water jacket agree with the measured values very well and that the temperature characteristics of these components exhibit the same tendency, namely, the temperatures of these components increase slowly from the very start and rise sharply at the early stage, and then gradually reach to the final temperature when the heat generation is in balance with the heat dissipation into the atmosphere. And it takes about 1 h for the front and rear bearings and stator and water jacket to reach a thermal equilibrium state, and the equilibration time (1 h) is relatively short compared with the total test process. In fact, the rotational speed of the spindle has great influence on the equilibrium time because the heat generation of the bearings and motor depends on the rotational speed. And the higher the rotational speed of the spindle is, the shorter the equilibrium time will be. Moreover, the temperatures measured by the experiment showed fluctuations due to the effect of the cooling system. Besides, the slopes of the stator and water jacket's temperature curves are larger than that of the rear and front bearings because the heat generated by the stator is larger than that of the bearings. Namely, the thermal equilibrium time of the stator and water jacket is shorter than that of the bearings.

Figure 28 illustrates a comparison of temperature histories measured, the calculated results considering TCR and without considering TCR. The bearing temperatures without considering TCR are about 12 and 11 °C lower than the measured values for the front and rear bearings, respectively. The heat generated by the bearings flows into the shaft and bearing housing. However, the TCRs of bearing/shaft and bearing/bearing housing play the role of restricting the heat flowing from the bearings to the shaft and bearing housing, which results in a higher local temperature of the heat source. Therefore, for the bearing (heat source), the heat generated by itself is difficult to flow into the shaft and bearing housing, and hence, the heat generated by the bearing is accumulated. And the greater the

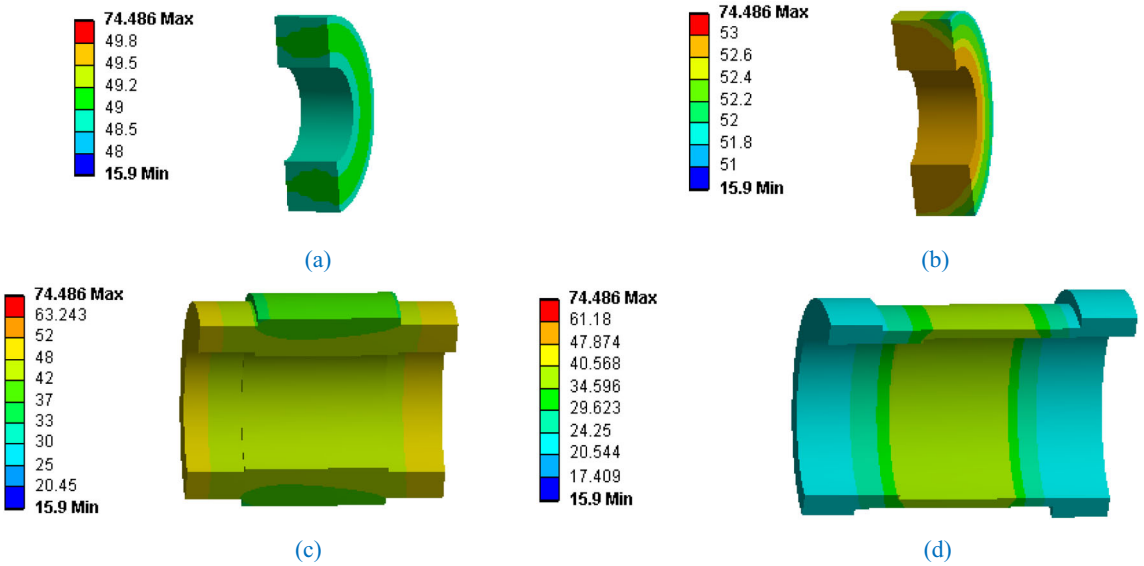

Fig. 26 Temperature contours of spindle components when thermal equilibrium: **a** rear bearing; **b** front bearing; **c** stator; **d** water jacket

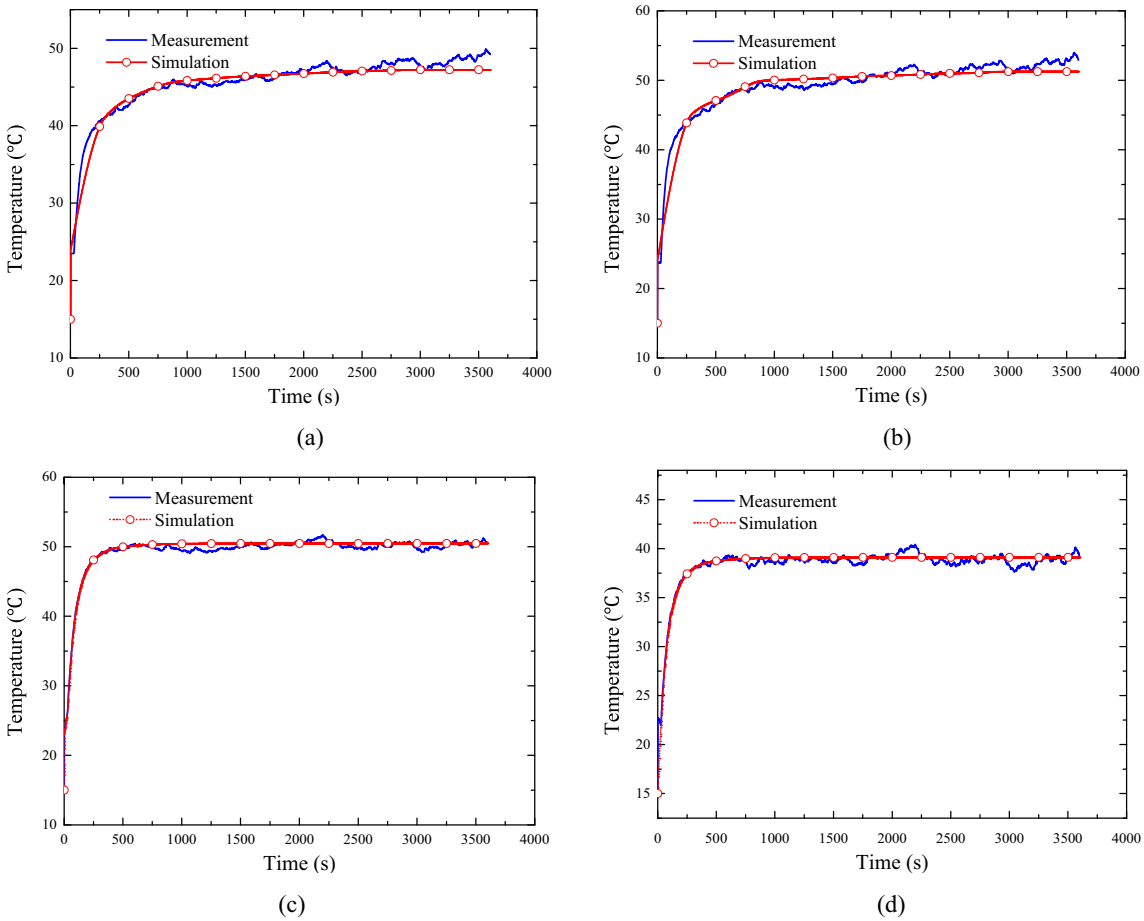

Fig. 27 Comparison of the temperature histories, simulated, experimental: **a** rear bearing; **b** front bearing; **c** stator; **d** water jacket

TCR, the greater the temperature difference between the two sides of the joint surface will be.

4.4.2 Thermal deformation analysis

Figure 29 shows the thermal deformation of the spindle system, magnified 250 times. The maximum deformation in the spindle system reaches 61.6 μm and occurs at *Y*+ end. The maximum deformations reach 57.8, 21.8, and 11.5 μm for the *X*, *Y*, and *Z* directions, respectively. The deformation at the left of the spindle is larger than that at the right. The fact that the temperature of the front bearing (the left) is higher than that of the rear bearing (the right) is the cause for the thermal deformation distribution.

To investigate the effect of thermal deformation on the machining accuracy, the comparison of thermal errors

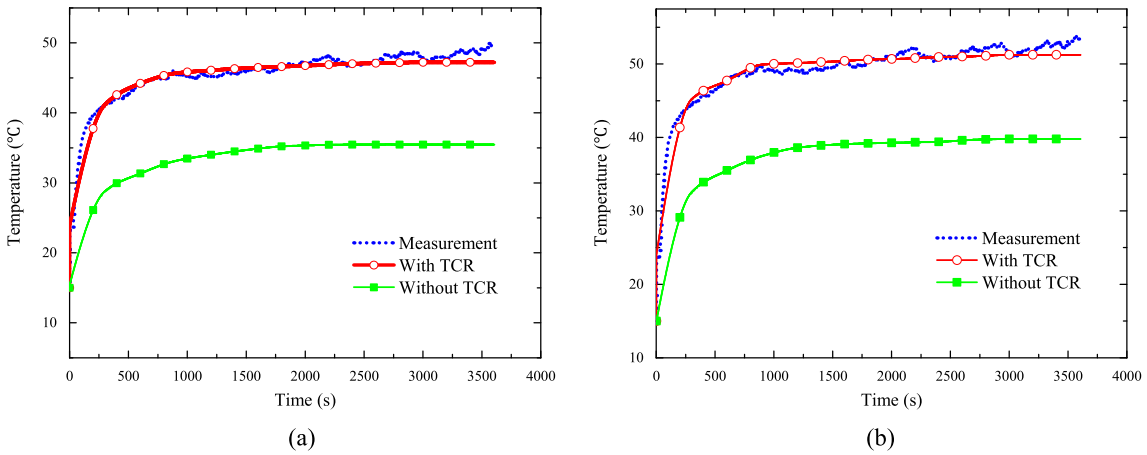

Fig. 28 Comparison of temperature experimental data with the simulation results: **a** rear bearing, **b** front bearing

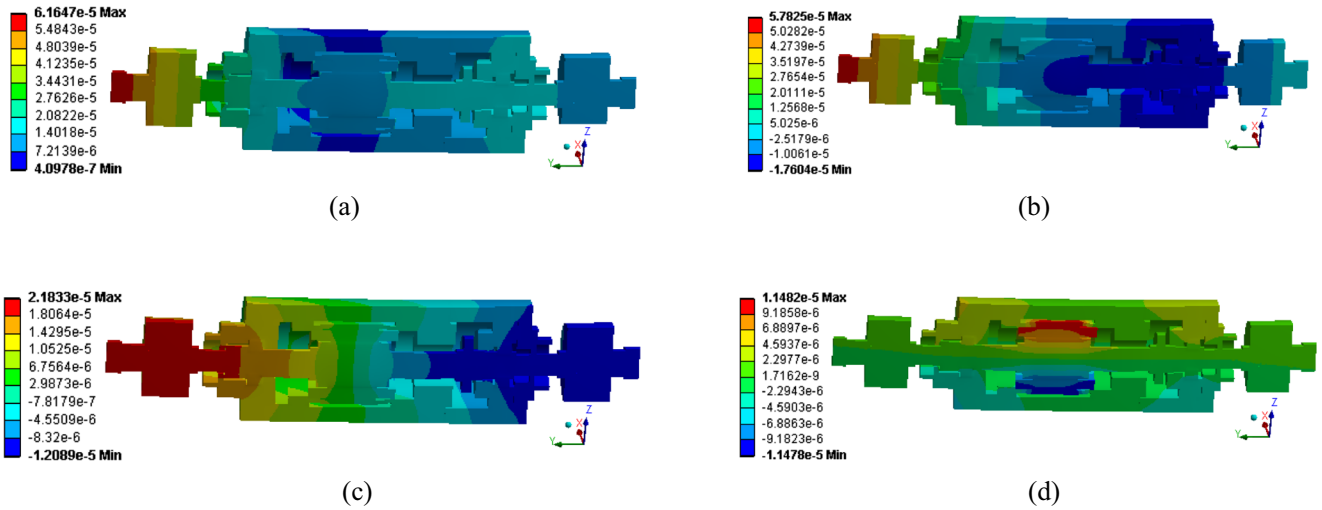

Fig. 29 Nephogram of thermal deformation when thermal equilibrium: **a** nephogram of total thermal deformation; **b** nephogram of total thermal deformation in *X*-direction; **c** nephogram of total thermal deformation in *Y*-direction; **d** nephogram of total thermal deformation in *Z*-direction

between experimental data and the simulation results is shown in Fig. 30. It can be seen that the deformation of *X*-direction is significant. This deformation may affect the machining accuracy seriously. At the same time, the deformation of *Y*-direction is also large, so the shaft will expand along the axial direction, which has a great effect on the machining precision.

The results of both models, one considering the TCRs and bearing stiffness and the other neglecting them, are illustrated in Fig. 31. As the TCRs of the bearing joints and bearing stiffness are considered, the values of deformations in the proposed model are much less than those in the model which ignores TCRs and bearing stiffness. The reason is as follows: the heat generated by the bearings flows into the shaft, and the flow of the heat from the bearings into the shaft is restricted by the resistance of TCR. Therefore, the amount of heat flowing into the shaft when TCR is considered is smaller than that into the shaft when TCR is ignored. Corresponding, the thermal deformations of *X*, *Y*, and *Z* directions are also smaller when TCR is considered.

It can be seen from the above discussion that the proposed model can predict the distribution of temperature field and the change of thermal deformation accurately from the cold to thermal equilibrium state, and it is much more accurate than the model which ignores TCRs and bearing stiffness.

5 Conclusions

A 3D FEA model, which considered TCRs and bearing stiffness, was proposed to conduct high-speed spindle transient thermal-structure analysis. Boundary conditions are determined by the following methods: the heat power of the

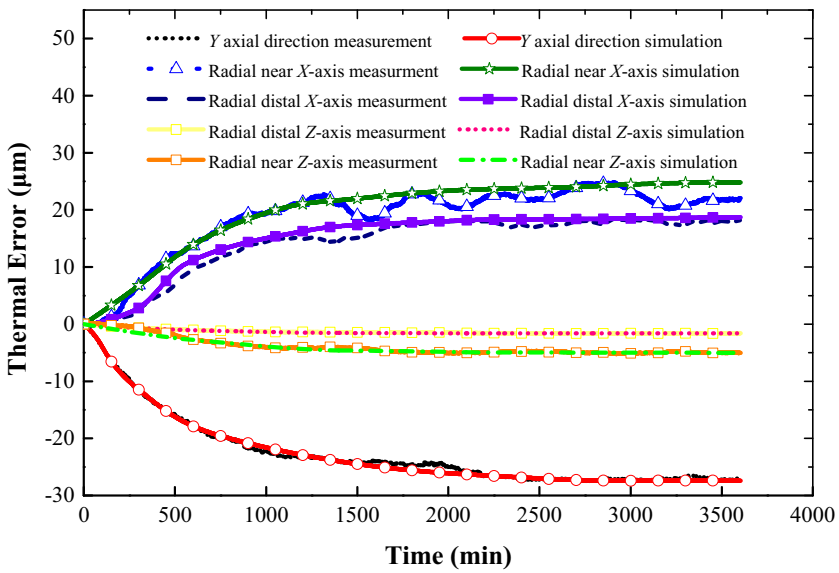

Fig. 30 Comparison between thermal errors of measurement data with simulation results

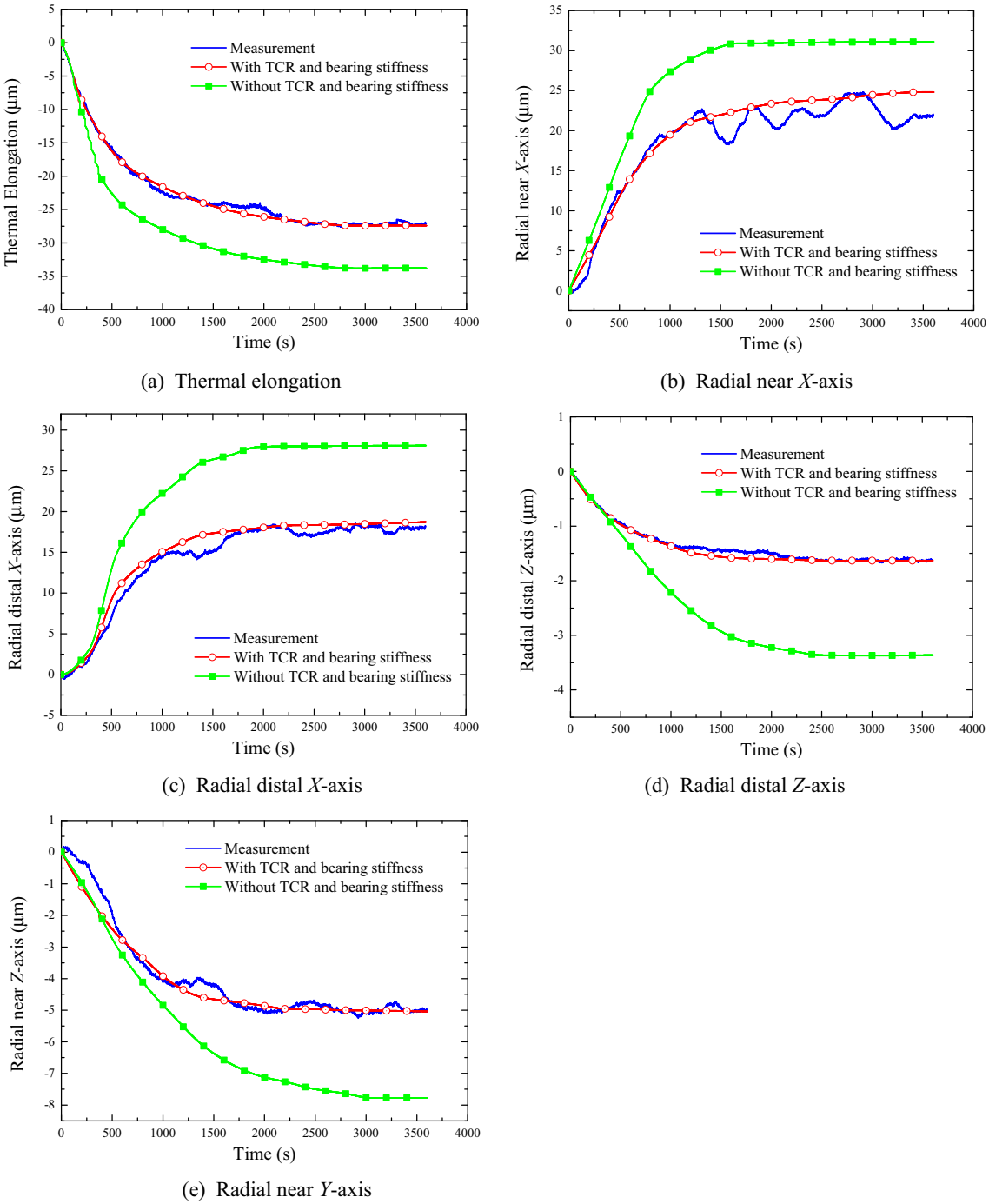

Fig. 31 Comparison of thermal errors of the measurement data with the simulation results with and without TCR. **a** Thermal elongation, **b** radial near *X*-axis, **c** radial distal *X*-axis, **d** radial distal *Z*-axis, **e** radial near *Y*-axis

built-in motor was calculated based on the efficiency analysis method; the Newton-Raphson algorithm was applied to compute heat generation and stiffness of bearings based on the quasi-static mechanics analysis of rolling bearing; the fluid flow state was determined by Reynolds number, and the convective heat transfer coefficients were calculated based on Nusselt number; a geometrical-mechanical-thermal model of TCR was proposed based on M-T fractal model, and the W-M function was utilized to characterize rough surface morphology; and the contact mechanics model was developed to calculate the contact parameters. The above boundary conditions were applied to the FEA model, and thermal equilibrium experiments were conducted to validate the effectiveness of the model. The results showed that the FEA model was much more accurate than traditional thermal analysis models without taking TCRs and bearing stiffness into account. Although

the model was developed for the analysis of a high-speed spindle system, it can also be used for thermal analysis of various machining systems, and the model of the TCR was suitable for fixed joints.

Acknowledgments This research is supported by the National High Technology Research and Development Program of China (Grant Number 2012AA040701).

Conflict of interest We declare that we have no financial and personal relationships with other people or organizations that can inappropriately influence our work; there is no professional or other personal interest of any nature or kind in any product or company that could be construed as influencing the position presented in, or the review of, the manuscript.

References

1. Bossmanns B, Tu JF (1999) A thermal model for high speed motorized spindles. Int J Mach Tools Manuf 39(9):1345–1366
2. Donmez MA, Hahn MH, Soons JA (2007) A novel cooling system to reduce thermally-induced errors of machine tools. Ann CIRP 56(1): 521–524
3. Bryan JB (1990) International status of thermal error research. Ann CIRP 39(2):645–656
4. Su H, Lu L, Liang Y, Zhang Q, Sun Y (2014) Thermal analysis of the hydrostatic spindle system by the finite volume element method. Int J Adv Manuf Technol 71(9–12):1949–1959
5. Liang Y, Su H, Lu L, Chen W, Sun Y, Zhang P (2014) Thermal optimization of an ultra-precision machine tool by the thermal displacement decomposition and counteraction method. Int J Adv Manuf Technol 1–11
6. Zivkovic A, Zeljkovic M, Tabakovic S, Milojevic Z (2014) Mathematical modeling and experimental testing of high-speed spindle behavior. Int J Adv Manuf Technol 1–16
7. Kim SM, Lee SK (2005) Spindle housing design parameter optimization considering thermo-elastic behavior. Int J Adv Manuf Technol 25(11–12):1061–1070
8. Babu SR, Raja VP, Thyla PR, Thirumalaimuthukumaran M (2014) Prediction of transient thermo-mechanical behavior of the headstock assembly of a CNC lathe. Int J Adv Manuf Technol 74(1–4):17–24
9. Zhang J, Feng P, Chen C, Yu D, Wu Z (2013) A method for thermal performance modeling and simulation of machine tools. Int J Adv Manuf Technol 68(5–8):1517–1527
10. Liu Z, Pan M, Zhang A, Zhao Y, Yang Y, Ma C (2014) Thermal characteristic analysis of high-speed motorized spindle system based on thermal contact resistance and thermal-conduction resistance. Int J Adv Manuf Technol 1–14
11. Su H, Lu L, Liang Y, Zhang Q, Sun Y, Liu H (2014) Finite element fractal method for thermal comprehensive analysis of machine tools. Int J Adv Manuf Technol 75(9–12):1517–1526
12. Kylander G (1995) Thermal modelling of small cage induction motors. Dissertation, Chalmers University of Technology
13. Harris TA (1991) Rolling bearing analysis. Wiley, New York
14. Jones AB (1960) A general theory for elastically constrained ball and radial roller bearings under arbitrary load and speed conditions. J Fluids Eng 82(2):309–320
15. Incropera FP (2011) Fundamentals of heat and mass transfer. Wiley, New York
16. Min X, Shuyun J, Ying C (2007) An improved thermal model for machine tool bearings. Int J Mach Tools Manuf 47(1):53–62
17. Gnielinski V, Kabalec S, Kind M, Martin H, Mewes D, Faber K, Stephan P (2006) VDI-Wärmeatlas. Springer, Berlin
18. Schmidt F (1967) Waermeuebergang und Druckverlust in Rohrschlagen. Chemische Ingenieur Technik 39
19. Mikić BB (1974) Thermal contact conductance: theoretical considerations. Int J Heat Mass Transfer 17(2):205–214
20. Yovanovich MM (1982) Thermal contact correlations. AIAA Paper 81–1164:83–95
21. Greenwood JA, Williamson JBP (1966) Contact of nominally flat surfaces. Proc R Soc Lond A 295(1442):300–319
22. Cooper MG, Mikic BB, Yovanovich MM (1969) Thermal contact conductance. Int J Heat Mass Transfer 12(3):279–300
23. McWaid TH, Marschall E (1993) A comparison of elastic and plastic contact models for the prediction of thermal contact conductance. Wärme Stoffübertragung 28(8):441–448
24. Berry MV, Lewis ZV (1980) On the Weierstrass-Mandelbrot fractal function. Proc R Soc Lond A 370(1743):459–484
25. Majumdar A, Tien CL (1991) Fractal network model for contact conductance. J Heat Transfer 113(3):516–525
26. Bhushan B, Majumdar A (1992) Elastic-plastic contact model for bifractal surfaces. Wear 153(1):53–64
27. Majumdar A, Bhushan B (1991) Fractal model of elastic-plastic contact between rough surfaces. J Tribol 113(1):1–11
28. ISO 230–3 (2007) Test code for machine tools—part 3: determination of thermal effects. Switzerland: ISO copyright office